

PNNL-32133

Discovering SPP Thermomechanical Pathways

October 2021

Anthony P Reynolds
Xiao Li
Md. Reza-E-Rabbi
Mageshwari Komarasamy
Glenn J Grant

DISCLAIMER

This report was prepared as an account of work sponsored by an agency of the United States Government. Neither the United States Government nor any agency thereof, nor Battelle Memorial Institute, nor any of their employees, **makes any warranty, express or implied, or assumes any legal liability or responsibility for the accuracy, completeness, or usefulness of any information, apparatus, product, or process disclosed, or represents that its use would not infringe privately owned rights.** Reference herein to any specific commercial product, process, or service by trade name, trademark, manufacturer, or otherwise does not necessarily constitute or imply its endorsement, recommendation, or favoring by the United States Government or any agency thereof, or Battelle Memorial Institute. The views and opinions of authors expressed herein do not necessarily state or reflect those of the United States Government or any agency thereof.

PACIFIC NORTHWEST NATIONAL LABORATORY
operated by
BATTELLE
for the
UNITED STATES DEPARTMENT OF ENERGY
under Contract DE-AC05-76RL01830

Printed in the United States of America

Available to DOE and DOE contractors from
the Office of Scientific and Technical
Information,
P.O. Box 62, Oak Ridge, TN 37831-0062
www.osti.gov
ph: (865) 576-8401
fox: (865) 576-5728
email: reports@osti.gov

Available to the public from the National Technical Information Service
5301 Shawnee Rd., Alexandria, VA 22312
ph: (800) 553-NTIS (6847)
or (703) 605-6000
email: info@ntis.gov
Online ordering: <http://www.ntis.gov>

Discovering SPP Thermomechanical Pathways

October 2021

Anthony P Reynolds
Xiao Li
Md. Reza-E-Rabbi
Mageshwari Komarasamy
Glenn J Grant

Prepared for
the U.S. Department of Energy
under Contract DE-AC05-76RL01830

Pacific Northwest National Laboratory
Richland, Washington 99354

Abstract

Friction extrusion is a thermomechanical process that combines conventional extrusion with the action of a rotating die. The plastic deformation of the material being sheared and extruded is the primary source of process heat and it produces strain distributions unlike those resulting from conventional extrusion. This paper proposes an improved strain analysis that evaluates three main strain components in a series of rate-controlled friction extrusions in which the steady state was achieved. Cylindrical AA1100 extrusion billets with two embedded markers were extruded to wire with a 10:1 diametral reduction. The shape change of the embedded markers was determined via serial, transverse sectioning and quantitative metallography of the extruded wires. Three mutually orthogonal strain components (longitudinal, circumferential, and radial) were calculated at different positions along each extruded wire from the marker's shape change. The development of strain from the initial transient to the steady state is discussed. The variation of the steady-state strain with different process parameters is correlated with the die advance per revolution.

Keywords: friction extrusion, plastic deformation, inserted marker, strain

1. Introduction

1.1. Background

Friction extrusion (FE) was invented by The Welding Institute in the UK in 1993 [1]. It combines the conventional extrusion process with the action of a rotating die and bypasses the external heating source. In the last decade, FE has received renewed interest for a variety of applications. A wide range of its derivative forms, like friction consolidation, friction stir back extrusion, and shear assisted processing and extrusion, are also emerging rapidly. A typical characteristic of these thermomechanical processes is that the process heat and plastic deformation are intrinsically coupled.

In contrast to conventional extrusion processes, in FE, the heat source is the energy dissipation of plastic deformation generated by the interaction between the billet and the rotating die. Hence, there are substantial differences between FE and conventional extrusion; these differences are leveraged to produce better extrudates or reduce the energy cost of manufacturing a product. The introduction of shear deformation makes FE ideologically close to severe plastic deformation processes like high pressure torsion [2], high pressure torsion extrusion [3], equal channel angular extrusion [4], and twist extrusion [5]. However, severe plastic deformation processes are mainly operated thermostatically at room temperature, so the processing speed must be low. In FE, however, deformation heat is favorable because the elevated temperature can reduce the required extrusion pressure and increase the processing speed.

The advantages of FE and its derivatives include the following: (a) It offers the capability to produce materials with better properties than those of otherwise equivalent conventionally extruded materials [6-9]. (b) With the potential to use lower processing temperatures (0.4 to 0.9 of the melting temperature) and span a wide range, FE enables the production of new functional materials and new phases unavailable from melting-based technologies like casting.

Alternatively, it can largely reduce the cost compared with the conventional manufacturing process [10, 11]. (c) When processing metal powders or machining waste, FE may enable higher production rates than powder metallurgy and melting processes, because it is a single-step, continuous shaping and forming technique [12-14]. (d) The required force [7] and energy consumption in solid phase processing are reported to be 20–50% lower than in remelt recycling processes [15, 16]. (e) The high shear deformation stirs and mixes material extensively when processing alloys or composite materials; this disperses the second-phase or filler material homogeneously in the matrix, avoiding degradation arising from segregation [17-19]. (f) The high shear deformation also reduces particle size by either mechanical comminution of insoluble particles or dissolution and reprecipitation of soluble phases, thus retaining or creating highly refined structures in materials [14, 20].

1.2 Understanding the deformation

To most effectively use FE to produce desired results, it is critical to understand the deformation, which also governs the heat generation. However, the complexity of the thermomechanically coupled process has impeded accurate mapping of the strain and temperature fields. Four characteristics make this challenging: (1) highly coupled plastic deformation and heat generation; (2) large gradients of deformation and temperature in both space and time domains; (3) unknown strains and strain rates, which are essential for describing heat generation in plasticity theory; (4) lack of accurate mechanical property data over the presumed large ranges of strain rate (10^{-1} – 10^2) and the wide temperature range (room temperature to near melting temperature) encountered in the process. An important first step

toward developing a comprehensive understanding of the process is to obtain the strains applied during FE and correlate these with process control parameters, including extrusion rate and die rotation rate.

The marker insert technique is a useful method for visualizing the material flow in solid phase processing. Seidel and Reynolds applied the marker insert technique in friction stir welding to visualize the material flow path after the tool had passed through the workpiece [21]. In that work, no attempt was made to quantify the strain or strain components; only qualitative information regarding the material flow path was obtained. Still, this was quite useful for comparison with various process simulations established by Xu et al. [22]. Valberg and Malvik first used marker studies in conventional extrusion to map material flow [23]. Valberg summarized the experimental techniques for characterizing large plastic deformations in hot extruded aluminum [24], including an internal stripe pattern technique and a three-dimensional grid pattern technique. Beygelzimer et al. also used fiber markers to investigate the material flow and strain tensors in twist extrusion [25]. However, use of the high-speed rotating die in FE greatly complicates the flow patterns as well as the resulting strains in the extruded part. Li et al. first performed a simple marker study in FE to estimate the strain in an AA6061 extrusion [26]. In this study, the marker material was tracked by serial sectioning of the extruded wire. Two strain components were evaluated: the longitudinal strain (governed exclusively by the reduction), and the in-plane strain. However, the in-plane strain was not a strict definition in continuum mechanics and it needed to be further resolved into the orthogonal directions of the coordinate system. In addition, the extrusion was performed in a force-controlled mode rather than extrusion rate-controlled mode because rate control was not possible with the uninstrumented extrusion device. The use of extrusion force control caused the extrusion rate to change continuously as uncontrolled heating of the billet occurred. Therefore, a steady-state condition was not reached. Moreover, process responses like force, torque, and temperature could not be collected. Consequently, it was not possible to accurately correlate the variations in imposed strain with the processing parameters. Nevertheless, the marker method used by Li et al. showed great promise for elucidating strain components in FE, and a similar methodology has been followed in this study.

Attempts have also been made to establish finite element models. Zhang et al. established pure thermal models [27] and thermomechanical models [28] of FE processes to study heat transfer and material flow phenomena. The thermomechanical models produced a reasonable pathway of material flow when compared to experimental observation. Because accurate strain and strain-rate information was lacking, the model was based on rather crude assumptions of the distribution in radius and depth of deformation and temperature. Therefore, the simulation does not predict or reproduce the experiments precisely.

In the present work, a more sophisticated, "one-of-a-kind" FE machine was used. It produces wires using extrusion rate control, so steady-state FE was achieved for the first time. Also, process responses that were not available in previous studies such as force, torque, power, and temperature were obtained. A series of experiments using cylindrical AA1100 extrusion billets with two embedded AA2050 markers was performed with different die rotational speeds and feed rates. The shape change of the embedded markers was determined via serial transverse sectioning and quantitative metallography of the extruded wires. From the marker shape change, a more rigorous and accurate strain analysis that derived three mutually orthogonal strain components (longitudinal, circumferential, and radial) was developed. The obtained strain was compared with the theoretical strain from conventional extrusion. A detailed parametric study of the relationship between the control parameters and the responses including strain, temperature, force, and torque will be discussed in a separate article.

2.0 Method

2.1 Experimental design

The extrusions in this study were performed using the Shear Assisted Processing and Extrusion (ShAPE) machine designed by Pacific Northwest National Laboratory and manufactured by BOND™ Technologies. Eight extrusion conditions were studied. The controlled parameters, i.e., die rotation rate, die advance rate, and die advance per die revolution (DAPR) for these eight extrusions are shown in Table 1.

Table 1. Process Control Parameters for Friction Extrusion

Extrusion #	Die rotation rate (rpm)	Die advance rate (mm/min)	Die advance per revolution (mm/revolution)
1	150	8	0.0533
2	300	8	0.0267
3	450	8	0.0178
4	300	4	0.0133
5	300	12	0.04
6	300	16	0.0533
7	300	40	0.1333
8	150	40	0.2667

In addition, process response parameters including extrusion pressure, torque, power, and temperature were recorded. A flat-faced MP159 (cobalt-nickel alloy) die was used for all extrusions. A thermocouple was inserted into a hole on the side of the die to measure the temperature at a point 0.5 mm from the die face and 5 mm radially from the center of the die. All extrusions were made with a 10:1 diametral reduction from a starting billet diameter of 25.4 mm to a final wire diameter of 2.54 mm. The initial billet length was 12.7 mm. The billet material was AA1100, commercially pure aluminum.

2.2 Strain measurement

The present study deals with the measurement of three orthogonal strain components in cylindrical coordinates (longitudinal, circumferential, and radial) during FE using an AA1100 aluminum billet as a matrix and AA2050 (aluminum-copper-lithium) wire as markers. Two longitudinal holes of 2.5 mm diameter were drilled through the billet, along the central axis and at 4.2 mm (that is, 1/3 of the radius of billet) from the central axis of the billet. AA2050 aluminum wires (2.54 mm in diameter) were pressed into the holes. The billet was put in a billet ring and placed in a water-cooled fixture, as shown in Fig. 1.

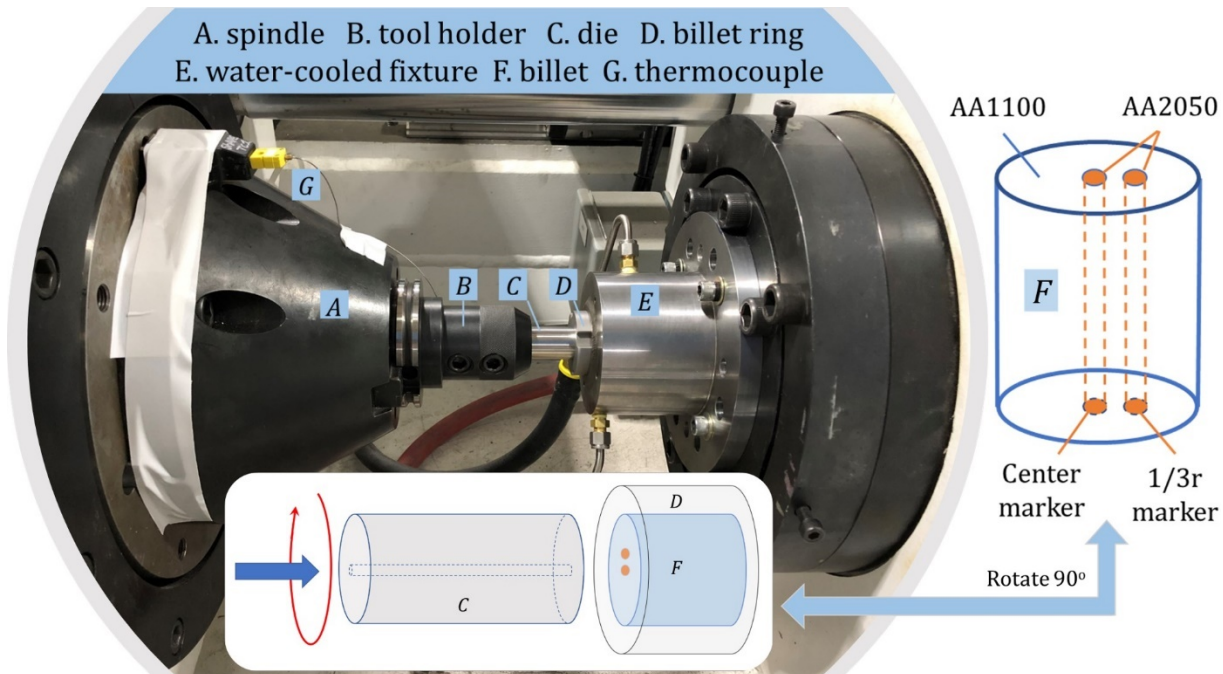


Fig. 1. Experimental setup (left) and schematic of AA1100 billet with inserted AA2050 markers (right).

After extrusion, the wires were sectioned transversely at longitudinal distances of 25 to 500 mm from the extrusion start. The cross sections were mounted, ground, polished, and etched using Keller’s reagent. Keller’s reagent was used because it creates excellent contrast between the AA2050 marker material and the AA1100 billet. The markers visible on each cross section were measured to inform calculations of the three strain components observable on the transverse section. The transverse cross-section images of 8 samples are presented in supplementary data figure 1.

Assume the main strain does not rotate at the steady-state[29], since the billet and extruded wire are cylindrical, the deformation on a wire cross section can be resolved into three components in cylindrical coordinates, as shown in Fig. 2: a longitudinal strain in the Z or extrusion direction, a radial strain, r , in the radial direction, and a circumferential strain, θ , in the die rotation direction. The strain of the marker can be expressed by the magnitude changes of the three cylindrical coordinates. The strains are written as follows:

$$\begin{aligned} \varepsilon_l &= \ln \left(\frac{A_0}{A_f} \right) \\ \varepsilon_r &= \ln \left(\frac{\bar{t}}{\bar{d}_0} \right) \\ \varepsilon_\theta &= \ln \left(\frac{l_f}{d_0} \right) \end{aligned}$$

Where ε_l , ε_r , and ε_θ are the longitudinal strain, radial strain, and circumferential strain, respectively. A_0 is the original cross-sectional area of the marker, A_f is the area of the marker on the transverse cross section of the extruded wire. \bar{t} is the average thickness of the marker in the radial direction, \bar{d}_0 is the average chord of the original marker-wire diameter ($\pi d_0/4$), l_f is the length of the marker in the theta (circumferential) direction, and d_0 is the original marker-wire diameter. As would be expected, the final shape of the extruded marker wire placed at the billet center and that at 1/3 of the billet radius are quite different. Fig. 2 shows the marker dimensions measured on a representative 1/3 r marker wire. For markers not at the center, the value of \bar{t} is

the average thickness of the spiral observed on the cross section. In most cases, the cross section of the marker wire on the central axis of the billet remains circular. It should be noted that because the three strain components measured on the transverse sections are mutually perpendicular, and the process is constant-volume plastic deformation, the components should sum to zero. It is not certain, however, that these are principal strain components.

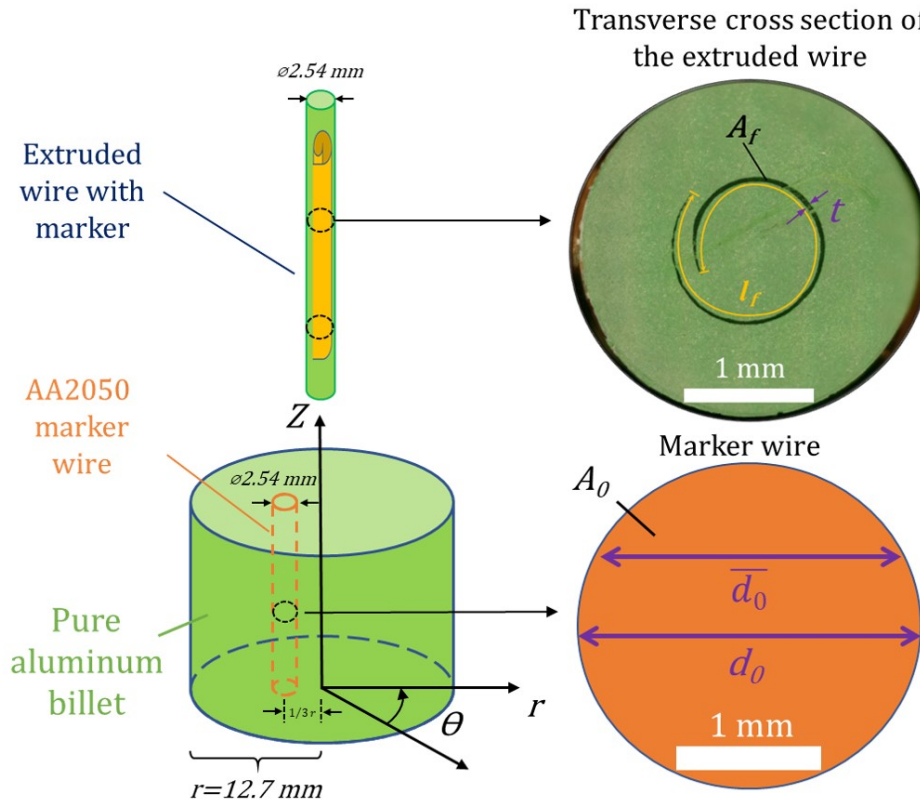


Fig. 2. Geometry and distribution of the 1/3 radius marker before and after FE.

3.0 Results

3.1 Process responses

The extrusion pressure, torque, and temperature as functions of processing time were measured for each extrusion. Fig. 3 shows the process data for two extrusions: one made at 150 rpm and one made at 450 rpm, both at 8 mm/min extrusion rate. These data are representative of what was observed in all the extrusions, although magnitudes of pressures, torques, and temperature vary somewhat with the specific process parameters. As each extrusion begins with the billet at room temperature, a temperature transient is observed, with the temperature becoming nearly steady by the end of the process. Over the course of each extrusion, the measured temperature ranged from 22°C at the start to between 550°C and 620°C at completion. This temperature variation drives the variation of other process responses. For each extrusion, required pressure is the highest at the beginning, falls as the temperature rises, reducing the billet flow stress, and finally achieves a nearly steady-state value. The observed torque follows a similar pattern. For all the extrusions that reached a temperature of 600°C or higher, the steady-state pressures were similar to each other, as were the torque values. The extrusions made with the higher DAPR generally had higher steady-state torque and pressure than those made with lower advance rates.

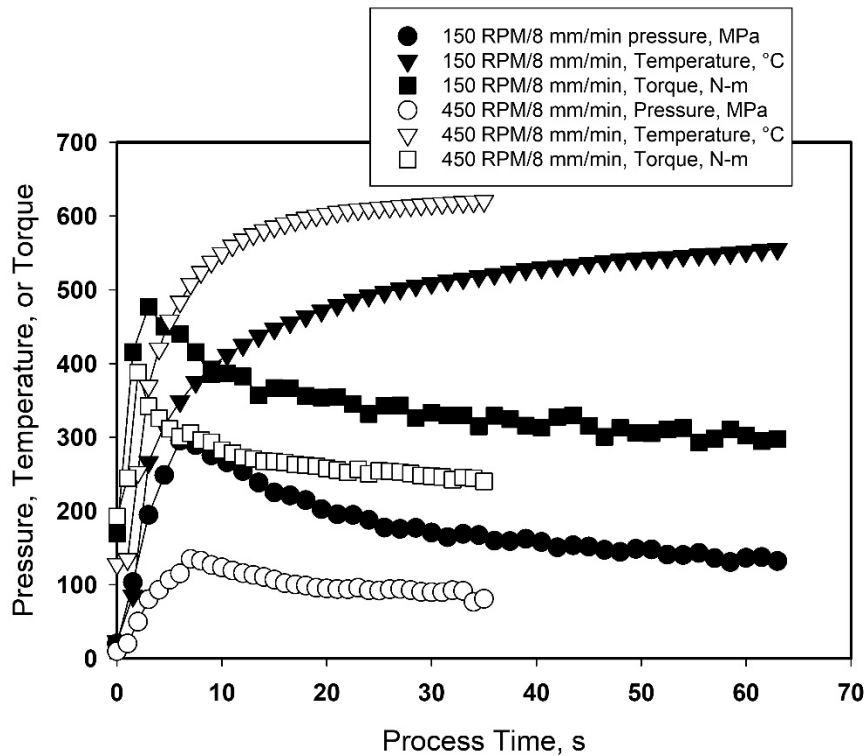


Fig. 3. Process responses for two extrusion conditions.

3.2 Measured strains

Fig. 4 shows etched wire cross sections for extrusions beyond the period of initial transient behavior (observed on some extrusions). The two cross sections are from wires made at (a) 150 rpm and a die advance rate of 8 mm/min and (b) 450 rpm and a die advance rate of 8 mm/min. Both cross sections were taken from the extruded wires at 0.25 m from the starting end of the extrusion. The AA2050 marker wires are readily distinguishable from the AA1100 billet material. In addition, it is apparent that the markers are continuous and well bonded with the AA1100

billet. This indicates that the markers flow compatibly with the billet material and that the deformation of the marker may be reliably assumed to be identical to the deformation of the billets. The spiral-like pattern of the 1/3 radials marker on the cross-section indicate their three-dimension geometry could be very similar to spiral layer structure observed in the high pressure torsion extrusion[3, 29].

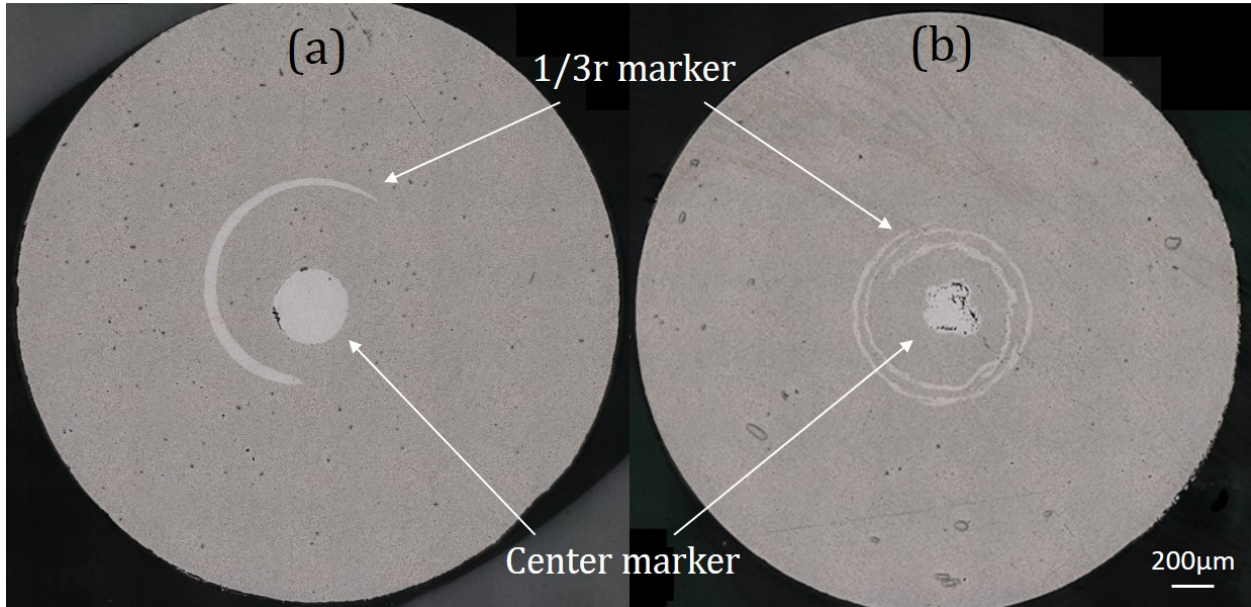


Fig. 4. Etched wire cross sections showing contrast between markers and billets. Both cross sections are from 0.25 m into the respective extrusions. Extrusions made at (a) 150 rpm and 8 mm/min die advance rate, (b) 450 rpm and 8 mm/min.

The appearance of the 1/3 r markers in the two cross sections shows that the imposed strain is different in the two conditions. In Figs. 5–7, the longitudinal, radial, and theta strains for each extrusion are presented as functions of the position along the wire (cross sections taken at different extrusion distances). The dashed lines in the figures indicate the respective strains expected for a “conventional” extrusion with a 10:1 diametral reduction.

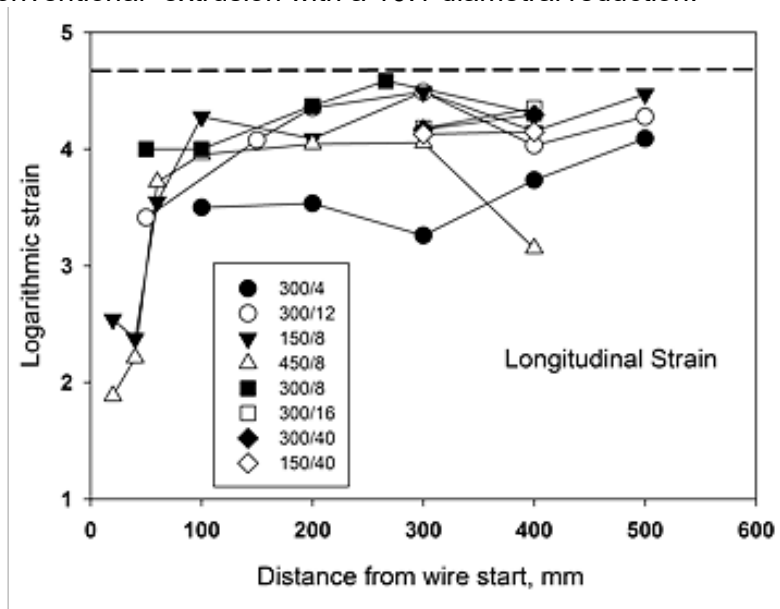


Fig. 5. Longitudinal strain in all eight extrusions. The key indicates the die rotation rate in rpm and the die advance rate in mm/min. The dashed lines indicate the respective strains expected for a “conventional” extrusion with a 10:1 diametral reduction.

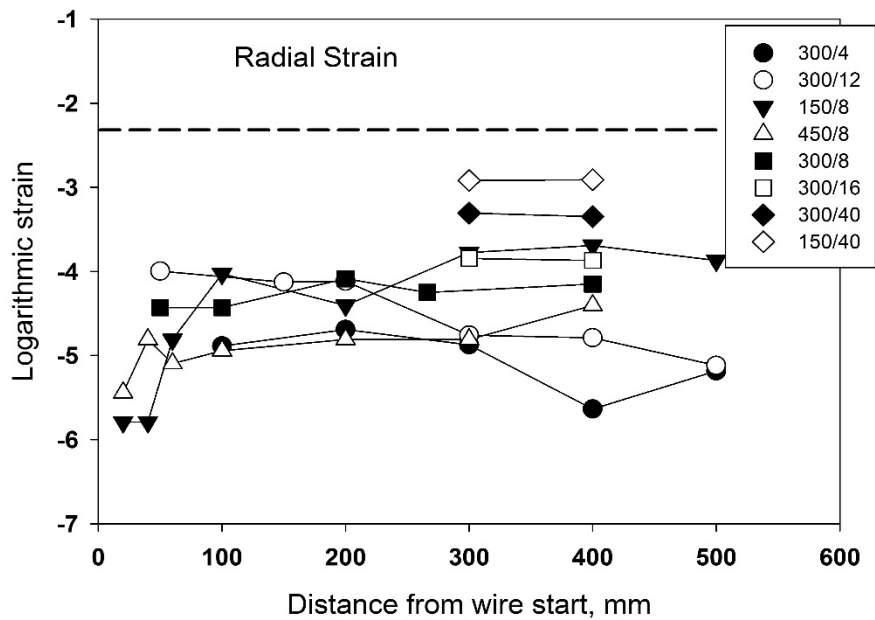


Fig. 6. Radial strain for all eight extrusions. The key indicates the die rotation rate in rpm and the die advance rate in mm/min.

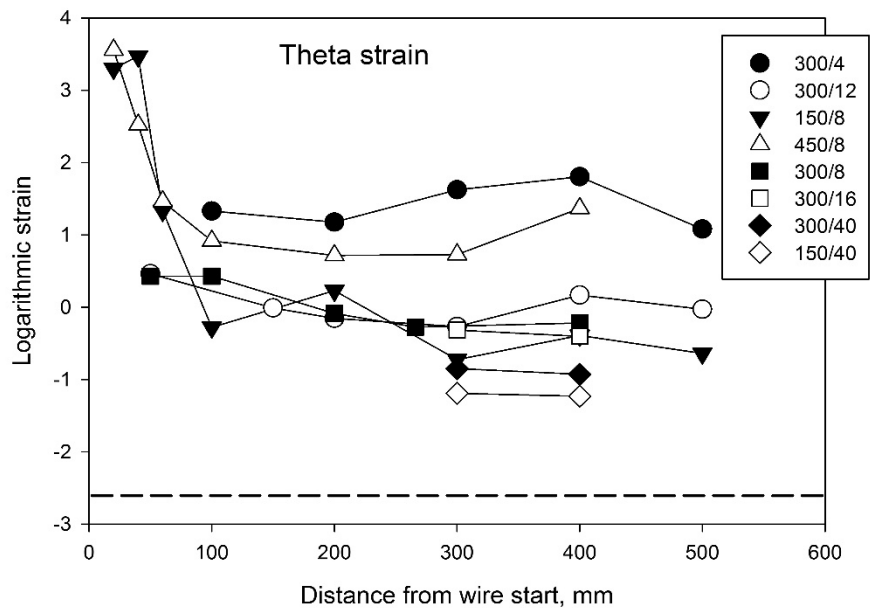
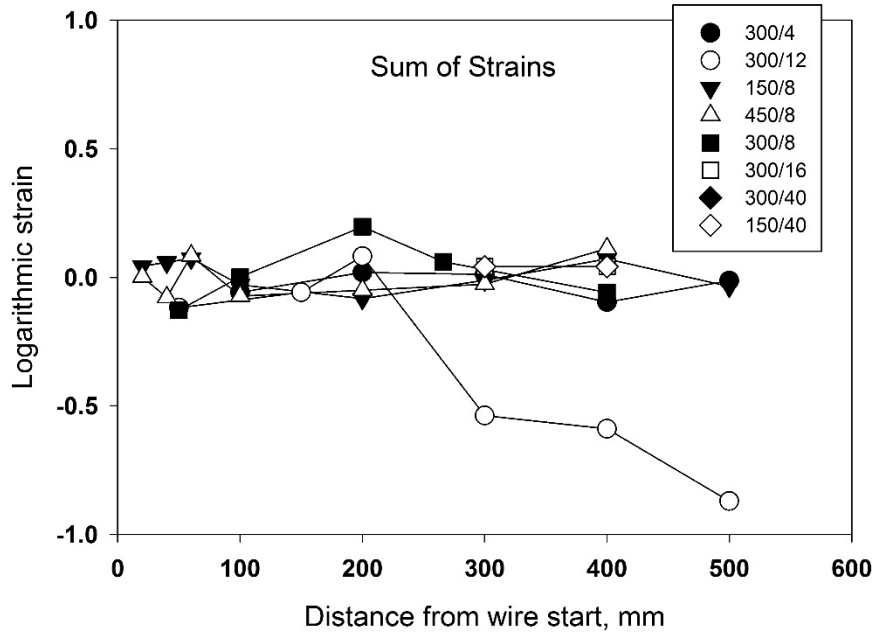


Fig. 7. Theta strain for all eight extrusions. The key indicates the die rotation rate in rpm and the die advance rate in mm/min.

As mentioned earlier, the sum of any three mutually orthogonal strain components measured during a constant-volume plastic deformation process should sum to zero. Fig. 8 shows the sums of the three strain components for each of the eight extrusions.

Fig. 8. Sums of the longitudinal, radial, and theta strain components for all eight extrusions.



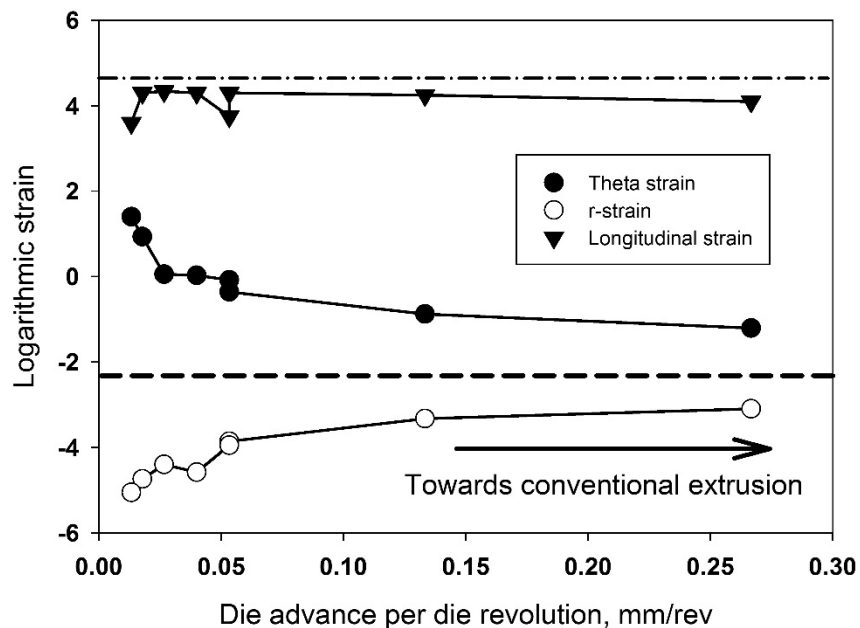
4.0 Discussion

The longitudinal strain values plotted in Fig. 5 for all eight extrusions as functions of the extruded wire length elucidate several points. In some cases, there is a transient region very close to the beginning of the extrusion where the observed longitudinal strain is quite low relative to the subsequent data points and far below the strain expected for an otherwise similar conventional extrusion (4.6 at 100:1 extrusion ratio). In all cases, after approximately 100 mm of extrusion, the values of strain are steady. The data are fairly well grouped and close to the value expected for an otherwise similar conventional extrusion, except for the extrusion made at 300 rpm and 4 mm/min. It is speculated that the transient observed near the start of some of the extrusions is related to the formation of a dead metal zone, and that at the beginning of the extrusion, the entire billet diameter is not feeding the extrusion. In the nearly steady-state region, after 100 mm of extrusion, low values of ϵ_l may be related to escape of billet material into the gap between the rotating die and the billet chamber (“flash,” similar to what is observed in some friction stir welds).

Figs. 6 and 7 show trends similar to those observed in Fig. 5 with respect to the existence of a transient followed by steady values of the strain components beyond the extrusion length of 100 mm. However, the radial and theta strains both show substantially greater dependence on the values of extrusion parameters than does the longitudinal strain. In addition, the strain values vary substantially from those that would be observed in an otherwise similar conventional extrusion (-2.3 for both radial and theta strains). Fig. 8, the sums of strains, shows that for nearly all cases, the sum of the three mutually orthogonal measured strains is very close to zero. This observation serves as an internal check on the accuracy of the measured strains. The results in Fig. 8 give confidence in the values shown in Figs. 5–7. Note that the scale in Fig. 8 spans a very narrow range, emphasizing small variations in the data.

To evaluate the effects of extrusion parameters on the measured strains, average values of the strains in the steady-state region for each extrusion are plotted against the corresponding DAPR in Fig. 9.

Fig. 9. Average value of each strain component vs. the corresponding die advance per revolution.



Several salient points are illustrated in Fig. 9. First, the longitudinal strain is independent of the extrusion parameters. This is not unexpected, because this component of strain should depend only on the overall extrusion reduction—in this case, 10:1. The longitudinal strain measured for all extrusions is close to the value expected for a conventional extrusion of the same reduction, 4.6, represented by the dot-dash line. For discussion of the theta and radial strains, it is important to note that increasing the value of DAPR is associated with extrusion parameters that approaches those of a conventional extrusion. The DAPR associated with a conventional extrusion is, of course, infinite, since the die advance rate is divided by a zero die rotation rate. The data for radial and theta strains indicate that (a) these strain components depend on the extrusion parameters as represented by the DAPR, (b) they do differ from each other, and (c) they can be quite far from the values expected for a conventional extrusion of the same reduction (i.e., -2.6, represented by the dashed line). As might be expected, the deviation from conventional extrusion is greatest at low DAPR. As DAPR increases, the values of both the radial and theta strain components converge toward each other and toward the value expected for a conventional extrusion. It is particularly instructive to examine the strain values for the two components at $DAPR = 0.0533$. The data for this DAPR value were obtained from two extrusions, made with (a) a die rotation rate of 300 rpm and 16 mm/min die advance rate and (b) a die rotation rate of 150 rpm and a die advance rate of 8 mm/min. Even though these two extrusion rates differ by a factor of two, the radial and theta strain components in the two extrusions are nearly identical. This indicates that the imposed strains are governed by the DAPR, at least in this range of conditions.

5.0 Summary and Conclusions

To better understand the deformation in the FE process, extrusion rate-controlled experiments with 10:1 reduction were successfully performed using a flat die and varying extrusion rate and DAPR by more than an order of magnitude. Two marker wires were inserted into the precursor billet to visualize the deformation and help calculate the strain. The measured geometry of the markers is limited to one plane, the transverse cross section. Therefore, only the orthogonal strain components can be derived. To acquire the shear components, a new marker design or imaging method is needed. Also, the marker advance per revolution in the wire should be investigated in future work.

The main conclusions of this research are highlighted here:

- (1) The method for obtaining values of three mutually orthogonal main strain components in the steady-state region of FE was developed. The validity of the technique is supported by the sums of strain data (strains sum to zero for nearly all cases) and consistency of values measured for a given extrusion condition (strain values attain a steady-state after an initial transient).
- (2) Critically, the DAPR does not affect the values of longitudinal strain, as expected, and the values of circumferential and radial strain depend mainly on the DAPR in this range of extrusion conditions. Also, as expected, the circumferential and radial strains converge toward the conventional strain value as DAPR is increased.

The obtained strain values pave a pathway to understanding the deformation and heat generation in FE. The results also provide data to investigate the effect of the control parameters on the process responses. Critically, the obtained results are useful to help establish and validate analytical and numerical models of friction-based extrusion processes.

Acknowledgments:

This research was supported by the Solid Phase Processing Science Initiative at Pacific Northwest National Laboratory. Pacific Northwest National Laboratory is operated by Battelle for the U.S. Department of Energy under contract DE-AC05-76RL01830.

References

- [1] Thomas WM, Nicholas ED, Jones SB. Forming metallic composite materials by urging base materials together under shear. Patent US5262123A, November 1993.
- [2] Zhilyaev AP, Langdon TG. Using high-pressure torsion for metal processing: Fundamentals and applications. *Progress in Materials Science*, 2008, 53(6): p. 893-979. <https://doi.org/10.1016/j.pmatsci.2008.03.002>.
- [3] Ivanisenko Y, Kulagin R, Fedorov V, Mazilkin A. High Pressure Torsion Extrusion as a new severe plastic deformation process. *Materials Science and Engineering: A*, 2016, 664: p. 247-256. <https://doi.org/10.1016/j.msea.2016.04.008>.
- [4] Segal WM. Engineering and commercialization of equal channel angular extrusion (ECAE). *Materials Science and Engineering: A*, 2004, 386(1): p. 269-276. <https://doi.org/10.1016/J.MSEA.2004.07.023>.

- [5] Beygelzimer Y, Varyukhin V, Synkov S, Orlov D. Useful properties of twist extrusion. *Materials Science and Engineering: A*, 2009, 503(1-2): p. 14-17.
- [6] Baffari D, Reynolds AP, Li X, Fratini L. Influence of processing parameters and initial temper on Friction Stir Extrusion of 2050 aluminum alloy. *Journal of Manufacturing Processes*, 2017, 28: p. 319-325. <https://doi.org/10.1016/j.jmapro.2017.06.013>.
- [7] Li X, Overman NR, Roosendaal TJ, Olszta MJ, Zhou C, Wang H, et al. Microstructure and mechanical properties of pure copper wire produced by shear assisted processing and extrusion. *JOM*, 2019, 71(12): p. 4799-4805. doi:10.1007/s11837-019-03752-w.
- [8] Joshi VV, Jana S, Li D, Garmestani H, Nyberg E, Lavender C. High Shear Deformation to Produce High Strength and Energy Absorption in Mg Alloys, in: *Magnesium Technology*, 2014, Springer. p. 83-88. https://doi.org/10.1007/978-3-319-48231-6_19.
- [9] Whalen S, Jana S, Catalini D, Overman N, Sharp J. Friction Consolidation Processing of n-Type Bismuth-Telluride Thermoelectric Material. *Journal of Electronic Materials*, 2016, 45(7): p. 3390-3399. <https://doi.org/10.1007/s11664-016-4454-0>.
- [10] Catalini D, Kaoumi D, Reynolds AP, Grant GJ. Dispersoid Distribution and Microstructure in Fe-Cr-Al Ferritic Oxide Dispersion-Strengthened Alloy Prepared by Friction Consolidation. *Metallurgical and Materials Transactions A*, 2015, 46(10): p. 4730-4739. <https://doi.org/10.1007/s11661-015-3059-1>.
- [11] Jiang X, Whalen SA, Darsell JT, Mathaudhu S, Overman NR. Friction consolidation of gas-atomized Fe Si powders for soft magnetic applications. *Materials Characterization*, 2017, 123: p. 166-172. <https://doi.org/10.1016/j.matchar.2016.11.026>.
- [12] Tang W, Reynolds AP. Production of wire via friction extrusion of aluminum alloy machining chips. *Journal of Materials Processing Technology*, 2010, 210(15): p. 2231-2237. <https://doi.org/10.1016/j.jmatprotec.2010.08.010>.
- [13] Tahmasbi K, Mahmoodi M. Evaluation of microstructure and mechanical properties of aluminum AA7022 produced by friction stir extrusion. *Journal of Manufacturing Processes*, 2018, 32: p. 151-159. <https://doi.org/10.1016/j.jmapro.2018.02.008>.
- [14] Whalen S, Olszta M, Roach C, Darsell J, Graff D, Rabby RD, et al. High ductility aluminum alloy made from powder by friction extrusion. *Materialia*, 2019, 6: p. 100260. <https://doi.org/10.1016/j.mtla.2019.100260>.
- [15] Duflou JR, Tekkaya AE, Haase M, Welo T, Vanmeensel K, Kellens K, et al. Environmental assessment of solid state recycling routes for aluminium alloys: can

- solid state processes significantly reduce the environmental impact of aluminium recycling? *CIRP Annals*, 2015, 64(1): p. 37-40.
<https://doi.org/10.1016/j.cirp.2015.04.051>.
- [16] Baffari D, Reynolds AP, Masnata A, Fratini L, Ingarao G. Friction stir extrusion to recycle aluminum alloys scraps: Energy efficiency characterization. *Journal of Manufacturing Processes*, 2019. 43: p. 63-69.
<https://doi.org/10.1016/j.jmapro.2019.03.049>.
- [17] Catalini D, Kaoumi D, Reynolds AP, Grant GJ. Friction Consolidation of MA956 powder. *Journal of Nuclear Materials*, 2013 442(1, Supplement 1): p. S112-S118.
<https://doi.org/10.1016/j.jnucmat.2012.11.054>.
- [18] Li X, Grant G, Zhou C, Wang H, Perry T, Schroth J. Copper-Graphite Composite Wire Made by Shear-Assisted Processing and Extrusion, in: *Friction Stir Welding and Processing X*, 2019, Springer. p. 163-169.
<https://www.springerprofessional.de/en/copper-graphite-composite-wire-made-by-shear-assisted-processing/16464058>.
- [19] Li X, Zhou C, Overman N, Ma X, Canfield N, Kappagantula K, et al. Copper carbon composite wire with a uniform carbon dispersion made by friction extrusion. *Journal of Manufacturing Processes*, 2021, 65: p. 397-406.
<https://doi.org/10.1016/j.jmapro.2021.03.055>.
- [20] Narvan M, Abdi Behnagh R, Shen N, Besharati Givi MK, Ding H. Shear compaction processing of SiC nanoparticles reinforced magnesium composites directly from magnesium chips. *Journal of Manufacturing Processes*, 2016, 22: p. 39-48. <https://doi.org/10.1016/j.jmapro.2016.01.010>.
- [21] Seidel TU, Reynolds AP. Visualization of the material flow in AA2195 friction-stir welds using a marker insert technique. *Metallurgical and Materials Transactions A*, 2001, 32(11): p. 2879-2884. <https://doi.org/10.1007/s11661-001-1038-1>.
- [22] Xu S, Deng X, Reynolds AP, Seidel TU. Finite element simulation of material flow in friction stir welding. *Science and Technology of Welding and Joining*, 2001, 6(3): p. 191-193. <https://doi.org/10.1179/136217101101538640>.
- [23] Valberg H, Malvik T. Metal flow in die channels of extrusion investigated by an experimental grid pattern technique. in *Proceedings of International Aluminium Extrusion Technology Seminar*, 1996, Aluminium Association Inc, & Aluminium Extruders Council. AIP Conference Proceedings 1960, 030011, 2018;
<https://doi.org/10.1063/1.5034854>.
- [24] Valberg HS. Experimental techniques to characterize large plastic deformations in unlubricated hot aluminum extrusion. *Key Engineering Materials*, 367, 2008, 17-24, <https://doi.org/10.4028/www.scientific.net/KEM.367.17>.

- [25] Beygelzimer Y, Reshetov A, Prokof'eva O, Synkov S. Kinematics of metal flow during twist extrusion investigated with a new experimental method. *Journal of Materials Processing Technology*, 2009, 209(7) p. 3650-3656. <https://doi.org/10.1016/j.jmatprotec.2008.08.022>.
- [26] Li X, Tang W, Reynolds AP, Tayon WA, Brice CA. Strain and texture in friction extrusion of aluminum wire. *Journal of Materials Processing Technology*, 2016, 229: p. 191-198. <https://doi.org/10.1016/j.jmatprotec.2015.09.012>.
- [27] Zhang H, Li X, Tang W, Deng X. Heat transfer modeling of the friction extrusion process. *Journal of Materials Processing Technology*, 2015, 221: p. 21-30. <https://doi.org/10.1016/j.jmatprotec.2015.01.032>.
- [28] Zhang H, Li X, Deng X, Reynolds AP. Numerical simulation of friction extrusion process. *Journal of Materials Processing Technology*, 2018, 253: p. 17-26. <https://doi.org/10.1016/j.jmatprotec.2017.10.053>.

Figure Captions

Fig. 1. Experimental setup (left) and schematic of AA1100 billet with inserted AA2050 markers (right).

Fig. 2. Geometry and distribution of the 1/3 radius marker before and after FE.

Fig. 3. Process responses for two extrusion conditions.

Fig. 4. Etched wire cross sections showing contrast between markers and billets. Both cross sections are from 0.25 m into the respective extrusions. Extrusions made at (a) 150 rpm and 8 mm/min die advance rate, (b) 450 rpm and 8 mm/min.

Fig. 5. Longitudinal strain in all eight extrusions. The key indicates the die rotation rate in rpm and the die advance rate in mm/min. The dashed lines indicate the respective strains expected for a “conventional” extrusion with a 10:1 diametral reduction.

Fig. 6. Radial strain for all eight extrusions. The key indicates the die rotation rate in rpm and the die advance rate in mm/min.

Fig. 7. Theta strain for all eight extrusions. The key indicates the die rotation rate in rpm and the die advance rate in mm/min.

Fig. 8. Sums of the longitudinal, radial, and theta strain components for all eight extrusions.

Fig. 9. Average value of each strain component vs. the corresponding die advance per revolution.

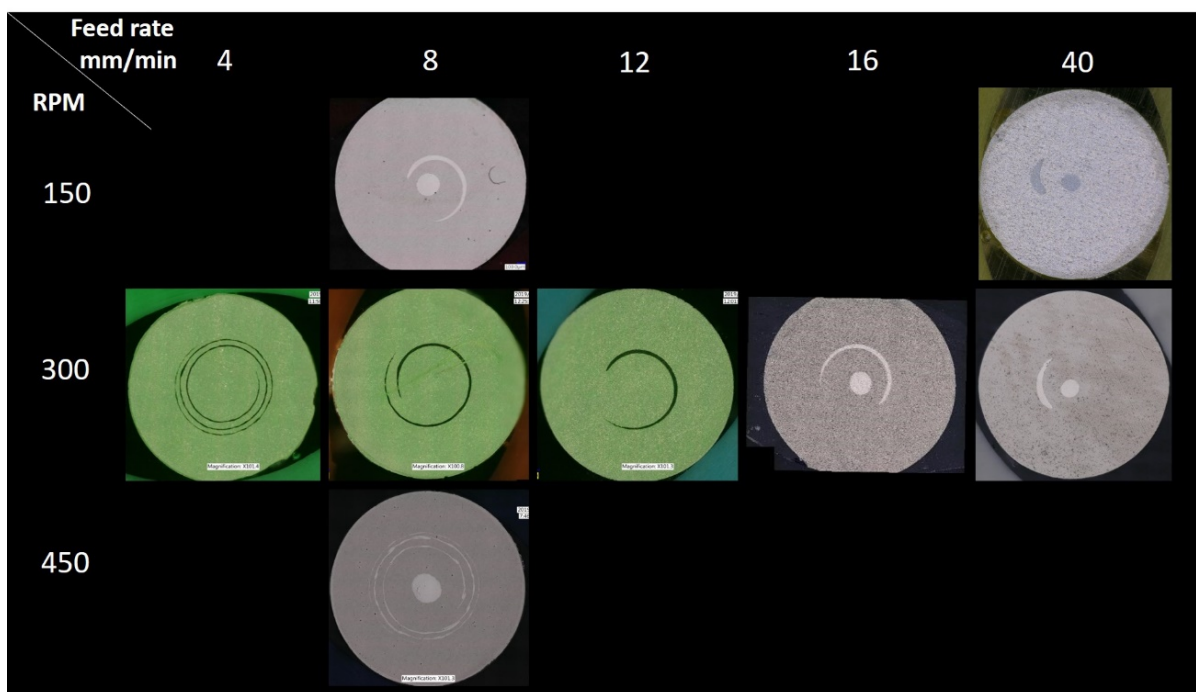
Table Caption

Table 1. Process Control Parameters for Friction Extrusion

1. Thomas, W.M., E.D. Nicholas, and S.B. Jones, *Forming metallic composite materials by urging base materials together under shear*. 1993, Google Patents.
2. Zhilyaev, A.P. and T.G. Langdon, *Using high-pressure torsion for metal processing: Fundamentals and applications*. Progress in Materials science, 2008. **53**(6): p. 893-979.
3. Ivanisenko, Y., et al., *High Pressure Torsion Extrusion as a new severe plastic deformation process*. Materials Science and Engineering: A, 2016. **664**: p. 247-256.
4. Segal, V.M., *Engineering and commercialization of equal channel angular extrusion (ECAE)*. Materials Science and Engineering: A, 2004. **386**(1): p. 269-276.
5. Beygelzimer, Y., et al., *Useful properties of twist extrusion*. Materials Science and Engineering: A, 2009. **503**(1-2): p. 14-17.
6. Baffari, D., et al., *Influence of processing parameters and initial temper on Friction Stir Extrusion of 2050 aluminum alloy*. Journal of Manufacturing Processes, 2017. **28**: p. 319-325.
7. Li, X., et al., *Microstructure and Mechanical Properties of Pure Copper Wire Produced by Shear Assisted Processing and Extrusion*. JOM, 2019. **71**(12): p. 4799-4805.
8. Joshi, V.V., et al., *High Shear Deformation to Produce High Strength and Energy Absorption in Mg Alloys*, in *Magnesium Technology 2014*. 2014, Springer. p. 83-88.
9. Whalen, S., et al., *Friction Consolidation Processing of n-Type Bismuth-Telluride Thermoelectric Material*. Journal of Electronic Materials, 2016. **45**(7): p. 3390-3399.
10. Catalini, D., et al., *Dispersoid Distribution and Microstructure in Fe-Cr-Al Ferritic Oxide Dispersion-Strengthened Alloy Prepared by Friction Consolidation*. Metallurgical and Materials Transactions A, 2015. **46**(10): p. 4730-4739.
11. Jiang, X., et al., *Friction consolidation of gas-atomized Fe Si powders for soft magnetic applications*. Materials Characterization, 2017. **123**: p. 166-172.
12. Tang, W. and A.P. Reynolds, *Production of wire via friction extrusion of aluminum alloy machining chips*. Journal of Materials Processing Technology, 2010. **210**(15): p. 2231-2237.

13. Tahmasbi, K. and M. Mahmoodi, *Evaluation of microstructure and mechanical properties of aluminum AA7022 produced by friction stir extrusion*. Journal of Manufacturing Processes, 2018. **32**: p. 151-159.
14. Whalen, S., et al., *High ductility aluminum alloy made from powder by friction extrusion*. Materialia, 2019. **6**: p. 100260.
15. Duflou, J.R., et al., *Environmental assessment of solid state recycling routes for aluminium alloys: can solid state processes significantly reduce the environmental impact of aluminium recycling?* CIRP Annals, 2015. **64**(1): p. 37-40.
16. Baffari, D., et al., *Friction stir extrusion to recycle aluminum alloys scraps: Energy efficiency characterization*. Journal of Manufacturing Processes, 2019. **43**: p. 63-69.
17. Catalini, D., et al., *Friction Consolidation of MA956 powder*. Journal of Nuclear Materials, 2013. **442**(1, Supplement 1): p. S112-S118.
18. Li, X., et al., *Copper-Graphite Composite Wire Made by Shear-Assisted Processing and Extrusion*, in *Friction Stir Welding and Processing X*. 2019, Springer. p. 163-169.
19. Li, X., et al., *Copper carbon composite wire with a uniform carbon dispersion made by friction extrusion*. Journal of Manufacturing Processes, 2021. **65**: p. 397-406.
20. Narvan, M., et al., *Shear compaction processing of SiC nanoparticles reinforced magnesium composites directly from magnesium chips*. Journal of Manufacturing Processes, 2016. **22**: p. 39-48.
21. Seidel, T.U. and A.P. Reynolds, *Visualization of the material flow in AA2195 friction-stir welds using a marker insert technique*. Metallurgical and materials transactions A, 2001. **32**(11): p. 2879-2884.
22. Xu, S.-w., et al., *Finite element simulation of material flow in friction stir welding*. Science and Technology of Welding and Joining, 2001. **6**(3): p. 191-193.
23. Valberg, H. and T. Malvik. *Metal flow in die channels of extrusion investigated by an experimental grid pattern technique*. in *PROCEEDINGS OF INTERNATIONAL ALUMINIUM EXTRUSION TECHNOLOGY SEMINAR*. 1996. ALUMINIUM ASSOCIATION INC, & ALUMINIUM EXTRUDERS COUNCIL.
24. Valberg, H.S. *Experimental techniques to characterize large plastic deformations in unlubricated hot aluminum extrusion*. in *Key Engineering Materials*. 2008. Trans Tech Publ.
25. Beygelzimer, Y., et al., *Kinematics of metal flow during twist extrusion investigated with a new experimental method*. Journal of Materials Processing Technology, 2009. **209**(7): p. 3650-3656.
26. Li, X., et al., *Strain and texture in friction extrusion of aluminum wire*. Journal of Materials Processing Technology, 2016. **229**: p. 191-198.
27. Zhang, H., et al., *Heat transfer modeling of the friction extrusion process*. Journal of Materials Processing Technology, 2015. **221**: p. 21-30.
28. Zhang, H., et al., *Numerical simulation of friction extrusion process*. Journal of Materials Processing Technology, 2018. **253**: p. 17-26.
29. Utyashev, F.Z., Y.E. Beygelzimer, and R.Z. Valiev, *Large and Severe Plastic Deformation of Metals: Similarities and Differences in Flow Mechanics and Structure Formation*. Advanced Engineering Materials, 2021: p. 2100110.

Supplementary data:



Supplementary data figure 1. Cross-section of friction extrusion wires made with different parameters.

Note: For some experiments done in the early stage of the study, center marker and 1/3 radius marker were used individually. Only 1/3 radius results are shown here.

Some Aspects of Machine Responses in Friction Extrusion

Md. Reza-E-Rabby,* Mechanical Engineer, Applied Materials and Manufacturing Group, Pacific Northwest National Laboratory, P.O. Box 999, Richland, WA, 99352.

Contact email: md.reza-e-rabby@pnnl.gov.

Xiao Li, Materials Scientist, Applied Materials and Manufacturing Group, Pacific Northwest National Laboratory, P.O. Box 999, Richland, WA, 99352.

Contact email: xiao.li@pnnl.gov.

Glenn Grant, Materials Scientist, Applied Materials and Manufacturing Group, Pacific Northwest National Laboratory, P.O. Box 999, Richland, WA, 99352.

Contact email: glenn.grant@pnnl.gov.

Suveen Mathaudhu, Professor at Metallurgical and Materials Engineering, Colorado School of Mines, Joint Appointee in Applied Materials and Manufacturing Group, Pacific Northwest National Laboratory, P.O. Box 999, Richland, WA, 99352.

Contact email: smathaudhu@mines.edu; suveen.mathaudhu@pnnl.gov.

Anthony Reynolds, Professor at Mechanical Engineering Department in University of South Carolina, Joint Appointee in Applied Materials and Manufacturing Group, Pacific Northwest National Laboratory, P.O. Box 999, Richland, WA, 99352.

Contact email: apr@sc.edu; anthony.reynolds@pnnl.gov.

Pacific Northwest National Laboratory

902 Battelle Boulevard
P.O. Box 999
Richland, WA 99354
1-888-375-PNNL (7665)

www.pnnl.gov